

Dissipative structures of diffuse molecular gas

III – Small-scale intermittency of intense velocity-shears[★]

P. Hily-Blant^{1,2}, E. Falgarone³, and J. Pety^{1,3}

¹ IRAM, Domaine Universitaire, 300 rue de la Piscine, F-38406 Saint-Martin-d'Hères

² Laboratoire d'Astrophysique, Observatoire de Grenoble, BP 53, F-38041 Grenoble Cedex 9

³ LRA/LERMA, UMR 8112, CNRS, Observatoire de Paris and École normale supérieure, 24 rue Lhomond, F-75231 Paris Cedex 05

Received / Accepted

ABSTRACT

Aims. We further characterize the structures tentatively identified on thermal and chemical grounds as the sites of dissipation of turbulence in molecular clouds (Papers I and II).

Methods. Our study is based on two-point statistics of line centroid velocities (CV), computed from three large ¹²CO maps of two fields. We build the probability density functions (PDF) of the CO line centroid velocity increments (CVI) over lags varying by an order of magnitude. Structure functions of the line CV are computed up to the 6th order. We compare these statistical properties in two translucent parsec-scale fields embedded in different large-scale environments, one far from virial balance and the other virialized. We also address their scale dependence in the former, more turbulent, field.

Results. The statistical properties of the line CV bear the three signatures of intermittency in a turbulent velocity field: (1) the non-Gaussian tails in the CVI PDF grow as the lag decreases, (2) the departure from Kolmogorov scaling of the high-order structure functions is more pronounced in the more turbulent field, (3) the positions contributing to the CVI PDF tails delineate narrow filamentary structures (thickness ~ 0.02 pc), uncorrelated to dense gas structures and spatially coherent with thicker ones (~ 0.18 pc) observed on larger scales. We show that the largest CVI trace sharp variations of the extreme CO linewidths and that they actually capture properties of the underlying velocity field, uncontaminated by density fluctuations. The confrontation with theoretical predictions leads us to identify these small-scale filamentary structures with extrema of velocity-shears. We estimate that viscous dissipation at the 0.02 pc-scale in these structures is up to 10 times higher than average, consistent with their being associated with gas warmer than the bulk. Last, their average direction is parallel (or close) to that of the local magnetic field projection.

Conclusions. Turbulence in these translucent fields exhibits the statistical and structural signatures of small-scale and inertial-range intermittency. The more turbulent field on the 30 pc-scale is also the more intermittent on small scales. The small-scale intermittent structures coincide with those formerly identified as sites of enhanced dissipation. They are organized into parsec-scale coherent structures, coupling a broad range of scales.

Key words. ISM: clouds, ISM: magnetic fields, ISM: kinematics and dynamics, turbulence

1. Introduction

Star formation proceeds *via* gravitational instability in dense gas, but the respective roles of turbulence and magnetic fields in that process are still debated issues (Ciolek & Basu 2006; Tassis & Mouschovias 2004; Mac Low & Klessen 2004; Padoan et al. 2001; Klessen 2001; Bate et al. 2002) in spite of dedicated observational studies of magnetic fields in molecular clouds (Matthews & Wilson 2000; Crutcher 1999) and extensive theoretical and numerical works devoted to characterizing the properties of the turbulence (Boldyrev et al. 2002; Padoan et al. 2003). A hybrid paradigm is taking shape, where turbulence dominates the diffuse ISM dynamics and magnetic fields gain importance as the scale decreases (Crutcher 2005). Turbulence and magnetic fields are recognized as powerful stabilizing agents in molecular clouds, and a critical issue remains, turbulence dissipation: where, when, and at which rate and scale does it occur?

A generic property of turbulent flows is the space-time intermittency of the velocity field. Intermittency is observed

in laboratory experiments of incompressible turbulence, in the atmosphere, and in the solar wind (see recent reviews by Anselmet et al. 2001; Bruno & Carbone 2005). It manifests itself *i)* as non-Gaussian tails in the probability distribution of all quantities involving velocity differences (*e.g.* gradient, shear, vorticity, rates of strain, and energy dissipation rate), *ii)* anomalous scaling of the high-order structure functions of the velocity increments (Anselmet et al. 1984), and *iii)* the existence of coherent structures of intense vorticity (Vincent & Meneguzzi 1991; Moisy & Jiménez 2004, hereafter MJ04). It has long been unclear whether these three manifestations, which refer either to the statistical properties of the flow or to its coherent structures, were related.

Statistical models make theoretical predictions in terms of the two-point statistics of the velocity field, with no link to any physical structures in the turbulent flow. In particular, the structure functions $S_p(l) = \langle [v(r+l) - v(r)]^p \rangle$ of the velocity field are expected to be power laws $S_p(l) \propto l^{\zeta(p)}$. As p increases, the structure functions give more weight to intense and rare events. In principle then, a detailed description of the velocity field could be achieved with the knowledge of all S_p for $p \rightarrow \infty$, however, the number of points N_p needed to compute S_p grows with p ,

Send offprint requests to: e-mail: philybla@obs.ujf-grenoble.fr

[★] Based on observations carried out with the IRAM-30m telescope. IRAM is supported by INSU-CNRS/MPG/IGN.

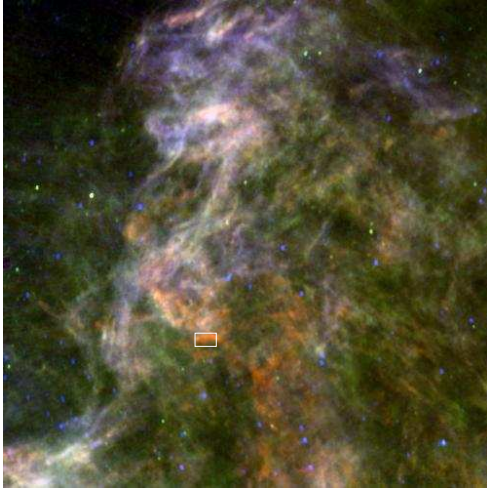


Fig. 1. Reprocessed IRAS map of the Polaris Flare (Miville-Deschênes & Lagache 2005). The map size is about $10^\circ \times 10^\circ$ or 27×27 pc. The parsec-scale field analyzed in this paper is shown as a white rectangle. The $100\mu\text{m}$, $60\mu\text{m}$ and $12\mu\text{m}$ emissions are red, green and blue respectively.

and an educated guess is $N_p \sim 10^{p/2}$. Fortunately, theoretical models show that, with a limited number of orders ($p > 3$), some properties of the turbulence can still be tested. The Kolmogorov theory of non-intermittent turbulence (hereafter K41, see *e.g.* Frisch 1995) predicts $\zeta(p) = p/3$, while experiments show a clear departure from this scaling, generally with $\zeta(p) < p/3$ for $p > 3$. The departure from the $p/3$ scaling is usually interpreted as a definition of intermittency. Statistical models predict intermittent scalings $\zeta(p) \neq p/3$. One such model (She & Lévy 1994, hereafter SL94, see Appendix A3) has an intermittent scaling $\zeta_p^{\text{SL}} = p/9 + 2[1 - (2/3)^{p/3}]$, in excellent agreement with tunnel-flow experimental data (Benzi *et al.* 1993).

The structural approach is inspired from laboratory experiments showing filaments of high vorticity (Douady *et al.* 1991). Localized regions of high vorticity and rate of strain (and thus energy dissipation) are found in numerical simulations at high resolution of both incompressible and compressible (Porter *et al.* 1994) and magneto-hydrodynamical (MHD) turbulence (Vincent & Meneguzzi 1991; Mininni *et al.* 2006b). Recently, MJ04 found that intense structures of vorticity and rate of strain are respectively filaments and ribbons that are not randomly distributed in space but that instead form clusters of inertial-range extent, implying a large-scale organization of the small-scale intermittent structures. In 1024^3 numerical simulations of incompressible turbulence, with variable large-scale stirring forces, Mininni *et al.* (2006a) have shown that the large and small-scale properties of the flow are correlated, namely that *i*) more intense small-scale gradients and vortex tubes are concentrated in the regions where the large-scale shears are the largest, and that *ii*) the departure from the Kolmogorov scaling is more pronounced in these regions. They infer from these results that the statistical signatures of intermittency are linked to the existence of the small-scale vortex tubes.

Investigations of interstellar turbulence are plagued by projection effects that affect our knowledge of the velocity. Direct inversion of the observations being a highly degenerate procedure, progress relies on astrophysical observables derived from numerical simulations of turbulence, and their confrontation to real data (see the review of Elmegreen & Scalo 2004). Along

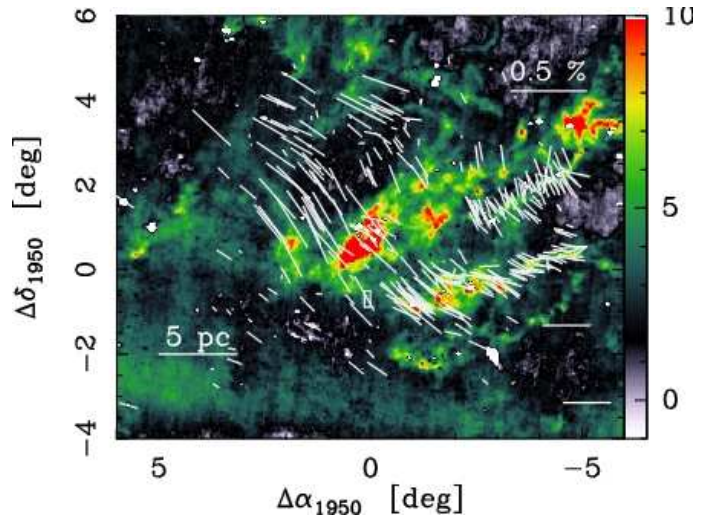


Fig. 2. Map of the cold dust emission in the Taurus molecular complex built from the reprocessed $60\mu\text{m}$ and $100\mu\text{m}$ IRAS maps (Hily-Blant *et al.* 2007b) following the method of Abergel *et al.* (1995). The orientation of the projection of the magnetic fields on the sky (Heiles 2000) is shown as white segments of length proportional to the polarization degree. The parsec-scale field discussed in this paper is centered at $\alpha_{2000} = 04^{\text{h}}40^{\text{m}}08.84^{\text{s}}$, $\delta_{2000} = 24^\circ12'48.40''$ and is shown as a white rectangle at offsets $(0^\circ, -1^\circ)$.

these lines, Lis *et al.* (1996) have shown that it is possible to trace the projection of the most intense velocity-shears with a measurable quantity based on two-point statistics of the velocity field: the line centroid velocity increments (CVI). This method, applied to different fields observed in CO lines, a star-forming region (Lis *et al.* 1998) and quiescent regions (Pety & Falgarone 2003, hereafter PF03) revealed filamentary structures unrelated with the gas mass distribution. The line centroid velocities (and their increments) are sensitive to optical depth effects and to density, temperature, and abundance fluctuations along the line of sight. Their relevance in any analysis of the statistical properties of the actual velocity fields have therefore been repeatedly questioned. Several recent studies have clarified the issue (Lazarian & Pogosyan 2000; Miville-Deschênes *et al.* 2003; Levrier 2004; Ossenkopf *et al.* 2006) without having provided any final answer to that question yet. The present work is part of a broad study in which we characterize the structures of largest CVI on thermal, chemical, and statistical grounds, and then repeat this analysis in different turbulent clouds. The goal of this broad program is to shed light on what these structures actually trace.

One of the two fields studied in this paper is the parsec-scale environment of two low-mass dense cores in the Polaris Flare. In the vicinity of the dense cores, Falgarone *et al.* (2006) (hereafter Paper I) find HCO^+ abundances locally far in excess of steady-state chemical predictions. The large measured abundances are consistent with a scenario that involves an impulsive heating of the gas, during which a warm chemistry is triggered, followed by a slow chemical and thermal relaxation. According to this scenario, the observed abundances and gas densities, in the range 200 and 600 cm^{-3} , correspond to a gas that has cooled down to 100–200 K. In Hily-Blant & Falgarone (2007a) (hereafter Paper II), we analyze the mass distribution of the gas in the environment of the dense cores and disclose

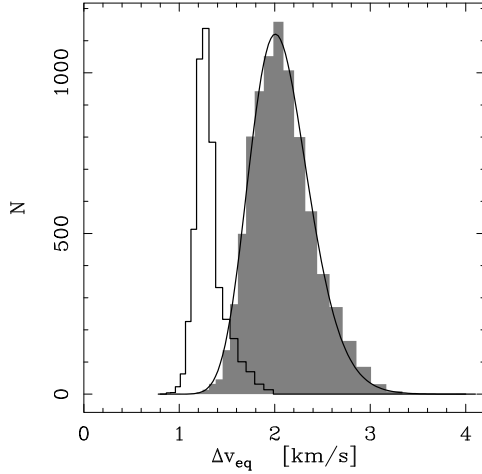


Fig. 3. Histograms of the equivalent width ($\Delta v_{\text{eq}} = \int T(v_x) dv_x / T_{\text{peak}}$) of the $^{12}\text{CO}(1-0)$ line in Polaris (shaded area) and Taurus. The result of the log-normal fit to the Polaris histogram is also shown.

localized regions where the ^{12}CO profiles exhibit broad wings. Multi-line analysis shows that gas in these linewidths is optically thin in the $^{12}\text{CO}(1-0)$ line and warmer than 25 K with density $< 1000 \text{ cm}^{-3}$. The new result is that this warm gas component is not widespread but localized in filaments. The dispersion of the orientation of the filaments of dense gas in the field, compared to the velocity dispersion, suggests that the turbulence in that field is trans-Alfvénic. In the forthcoming and last paper (Falgarone et al. 2008), we will report $^{12}\text{CO}(1-0)$ IRAM-Plateau de Bure observations performed in this field, revealing milliparsec-scale structures with large velocity-shears.

The present paper is dedicated to the statistical and structural analysis of turbulence in similar parsec-scale translucent samples of gas, which belong to two different large-scale environments: one, far from virial balance and devoid of stars, is the above-mentioned field in the Polaris Flare; the other lies at the edge of the Taurus-Auriga molecular complex. The statistical analysis is based on two-point statistics of the CO line emission observed at high spectral resolution, and the structural analysis consists in characterizing the regions of largest line-centroid velocity increments.

After presenting the data in Section 2, the characteristics of the turbulence in these two fields are derived based on the PDF of line CVI and structure functions (Section 3). We then show, in Section 4, that the regions of largest CVI on small-scales are filaments uncorrelated with the distribution of matter, but correlated with the filaments of gas optically thin in $^{12}\text{CO}(1-0)$ where large HCO^+ abundances are found. It is shown that these filaments remain coherent at the parsec-scale. In Section 5, we show that the ensemble of results, based either on the statistical or structural approach, provides a consistent description of the intermittency of turbulence in these two fields. In Section 6, the comparison of the radiative cooling of these structures with the fraction of the turbulent energy susceptible to being dissipated there further supports the proposition that the filaments of largest CVI somehow trace extrema of velocity-shear in the fields and pinpoint the sites of intermittent dissipation of turbulence.

Table 1. Dispersions $\sigma_{\delta C}$ (in km s^{-1}) of the PDF of CVI computed from the $^{12}\text{CO}(1-0)$ transition in the Polaris and Taurus fields for different lags l (in pixels).

l		$\sigma_{\delta C}$	
[pixels]	[pc]	Polaris km s^{-1}	Taurus km s^{-1}
3	0.02	0.11	0.05
6	0.05	0.17	0.07
9	0.07	0.22	0.09
12	0.09	0.25	0.10
15	0.11	0.27	0.11
18	0.14	0.29	0.12
18 ^(a)	0.14	0.30	—
36 ^(a)	0.27	0.46	—
54 ^(a)	0.41	0.57	—
72 ^(a)	0.54	0.64	—
90 ^(a)	0.68	0.69	—
108 ^(a)	0.81	0.72	—

(a) Computed from the KOSMA $^{12}\text{CO}(2-1)$ data of Bensch et al. (2001), where one pixel corresponds to 6 pixels of the IRAM data. The adopted distance is 150 pc for both fields.

2. Observations

2.1. Polaris field

Paper II describes the observations and data reduction of the IRAM ^{12}CO and $^{13}\text{CO}(1-0)$ and $(2-1)$ maps of the molecular cloud MCLD 123.5+24.9 located in the Polaris Flare. The location of the field mapped is shown in Fig. 1. The fully-sampled $\approx 1 \text{ pc} \times \text{pc}$ maps cover the non-star-forming translucent environment of two dense cores (Gerin et al. 1997; Falgarone et al. 1998; Heithausen 2002), corresponding to ≈ 3000 independent spectra (*i.e.* spaced by one beamsize or $20''$ at 115 GHz). The spectral resolution is 0.055 km s^{-1} . Since the signal-to-noise ratio of the $J = 2-1$ data is insufficient, only the $J = 1-0$ transition are used in the present paper. For comparison with larger scale properties, we use the fully-sampled $^{12}\text{CO}(2-1)$ data from Bensch et al. (2001) obtained at a lower angular resolution ($HPBW = 120''$) with the 3m KOSMA antenna.

2.2. Taurus field

The second field is located at the edge of the Taurus-Auriga molecular complex (Fig. 2). Observations were done with the IRAM-30m telescope. Observational strategy and data reduction are similar to those of the Polaris field. The maps, centered at ($\alpha_{2000} = 04^{\text{h}}40^{\text{m}}08.84^{\text{s}}$, $\delta_{2000} = 24^{\circ}12'48.40''$), are fully sampled in ^{12}CO and $^{13}\text{CO}(1-0)$. The data will be presented in more detail in a later paper (Hily-Blant & Falgarone 2008) but here we give the properties relevant to the present work. A total of 1200 independent spectra was obtained with the same spectral resolution of 0.055 km s^{-1} . In a small region (around $0,0''$ offsets in the map of Fig. 9), spectra show two separate components (at $v_{\text{LSR}} \approx 5$ and 10 km s^{-1}), and the analysis presented in this paper focuses on the main component at $v_{\text{LSR}} \approx 5 \text{ km s}^{-1}$, by blanking out the area corresponding to the high-velocity component.

2.3. Comparison of the two fields

Both fields are translucent. The visual extinction lies between $A_V = 0.6$ and 0.8 mag at a resolution of $8'$ in the Polaris field

(Cambr sy et al. 2001) and between $A_V = 1$ and 1.2 mag in the Taurus field at the same resolution (Cambr sy 1999). As shown in Fig. 3, the most probable equivalent width ($\Delta v_{\text{eq}} = \int T(v_x) dv_x / T_{\text{peak}}$, x being the coordinate along the line of sight) of the $^{12}\text{CO}(1-0)$ line is a factor two larger in Polaris than in Taurus. However, since the lines are stronger in the Taurus field, the integrated intensities in both fields are similar. Not only is the equivalent width larger in the Polaris field than in the Taurus one, but so is the dispersion of these equivalent widths. This factor 2 between the equivalent width translates into a factor 4 in the specific kinetic energy ratio between the two fields. The distribution of the equivalent width in Polaris is also very well-fitted by a log-normal distribution centered at $\Delta v_{\text{eq}} = 2 \text{ km s}^{-1}$ with dispersion 1.2 km s^{-1} . The parsec-scale velocity gradients, deduced from the centroid velocity maps, in the Polaris field ($\approx 2 \text{ km s}^{-1} \text{ pc}^{-1}$) is also twice larger than in the Taurus field.

These two parsec-scale fields are similar with respect to their size and average column density but have specific kinetic energies that differ by a factor 4. Moreover, they belong to two very different environments on the scale of $\sim 30 \text{ pc}$, that of Figs. 1 and 2. The total gas mass $M_{\text{tot}} = 4.4 \times 10^4 M_\odot$ at the scale of 30 pc is close to the virial mass in the Taurus-Auriga field (Ungerrechts & Thaddeus 1987), while it is more than six times lower in the Polaris Flare, $M_{\text{tot}} = 5500 M_\odot$ with $M_v = 3.6 \times 10^4 M_\odot$ (Heithausen & Thaddeus 1990). It is interesting that the virial masses of the two large-scale fields are close, because their velocity dispersion on the scale of 30 pc are similar, 3.8 and 4.8 km s^{-1} , respectively.

In summary, the less turbulent parsec-scale field lies on the far outskirts of the virialized Taurus-Auriga molecular complex, while the more turbulent field belongs to a much less massive complex, far from virial balance.

3. Two-point statistics of the centroid velocity

3.1. Probability density functions of the line centroid velocity increments

Following Lis et al. (1996), we analyze the two-point statistics of the centroid of the line-of-sight projection of the velocity v_x , which we note as $C(y, z) = C(\mathbf{r})$, where (y, z) is the position on the sky:

$$C(\mathbf{r}) = \int T(\mathbf{r}, v_x) v_x dv_x / \int T(\mathbf{r}, v_x) dv_x. \quad (1)$$

Increments of the centroid velocity between 2 points separated by l are defined by $\delta C(\mathbf{r}, l) = C(\mathbf{r} + l) - C(\mathbf{r})$. This quantity will be called centroid velocity increment (CVI). The main difficulty of this method concerns the computation of C , which not only depends on the bounds of the integrals in Eq. 1, but is also affected by the signal-to-noise ratio (SNR). To circumvent the bias introduced by spatial noise variations, Rosolowsky et al. (1999) degrade all the spectra to a unique threshold SNR. A different approach (PF03) has been adopted here, which uses the SNR of the integrated area as the optimization criterion to determine the spectral window used to compute C . The reason is that we have checked that the noise is already homogeneous in the data cubes, mostly as a result of the observing strategy consisting in several coverages of individual sub-maps in perpendicular directions.

For a given value of $l = |l|$, we compute maps of CVI for each direction l/l . A probability density function (PDF) is built from these maps by normalizing the histogram of CVI to a unit area. We thus obtain a PDF for each l and each direction. For each l ,

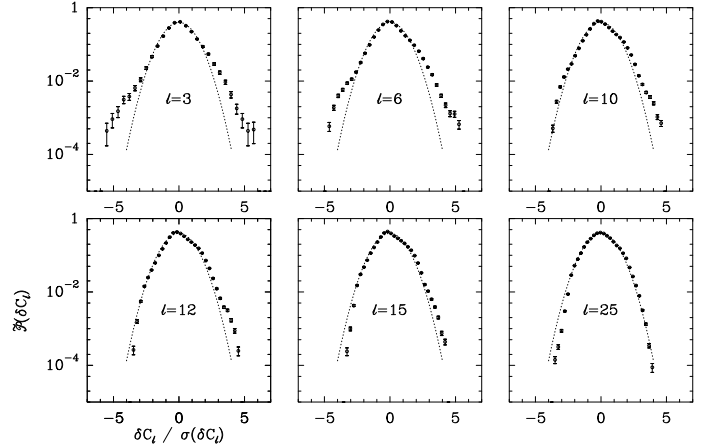


Fig. 4. Normalized PDF, $\mathcal{P}_n(\delta C_l)$, of the centroid velocity increments (CVI) computed from the $^{12}\text{CO}(1-0)$ IRAM map in Polaris. The PDF are computed for different lags between pairs of points: $l = 3$ to 25 pixels, and normalized to unity dispersion, such that the x -axis is in units of the rms $\sigma_{\delta C}$ for each distribution. Only the bins containing more than 10 data points were kept. The values of the dispersion $\sigma_{\delta C}$ are given in Table 1. A Gaussian of unit dispersion is also shown (dotted curve).

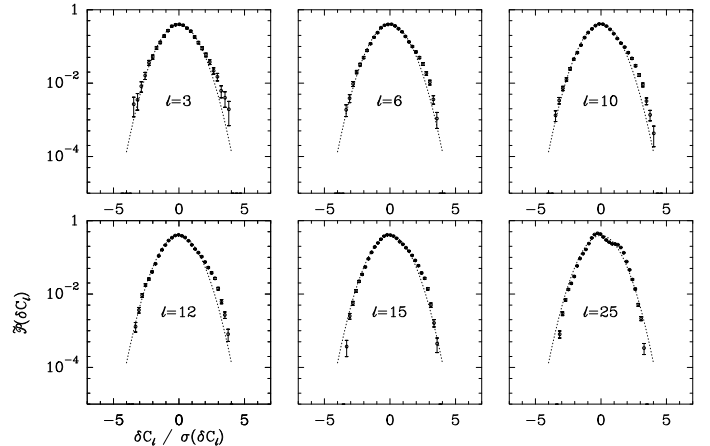


Fig. 5. Same as Fig. 4 for the $^{12}\text{CO}(1-0)$ data towards the Taurus field.

a PDF is computed with the CVI from all directions l/l , which we denote as $\mathcal{P}(\delta C_l)$. In order to get PDF with zero average and unit standard deviation and to ease the comparisons, we use the normalized PDF $\mathcal{P}_n(\delta C_l)$. All bins of the $\mathcal{P}_n(\delta C_l)$ associated to a number of points less than a given value N_{min} are blanked (see Appendix A.1). In the following, all $\mathcal{P}_n(\delta C_l)$ have 32 bins, and the adopted minimum number of data points for a bin to be significant is $N_{\text{min}} = 10$. In a second step, for a given l , we compute the azimuthal average of the absolute value of the CVI, resulting in a single CVI map. In practice the structures seen in the non-averaged maps are not smeared out, though they appear thinner in some cases.

Figs. 4 and 5 show the $\mathcal{P}_n(\delta C_l)$ computed for various lags from $l = 3$ to 25 pixels in the Polaris and Taurus fields, respectively. The lag $l = 3$ is the shortest distance between two independent points (since the sampling is half the beam size), and

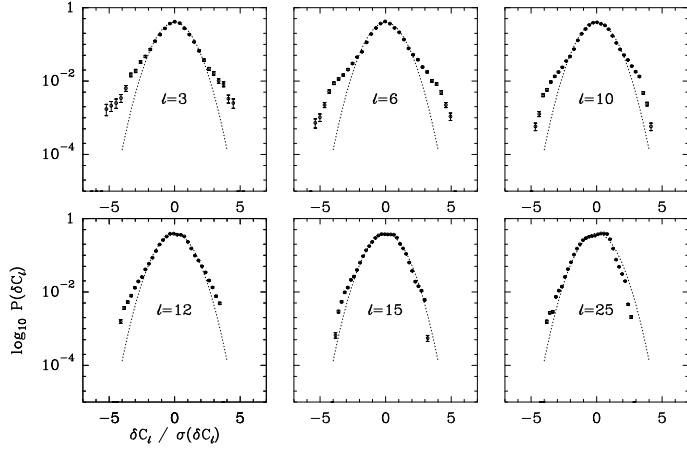


Fig. 6. Same as Fig. 4 for the $^{12}\text{CO}(2-1)$ KOSMA data from Bensch *et al.* (2001).

$l = 25$ corresponds to the largest lag with significant number of pairs of points. The number of data points corresponding to the three most extreme bins for $l = 3$ and 25 are in the range 12 – 50 and 20 – 500, respectively.

The PDF at large lags ($l > 15$) (Fig. 4) are nearly Gaussian and become slightly asymmetrical at $l = 12$, an effect we attribute to large-scale velocity gradients. Such effects cancel out at lags smaller than the characteristic scale of these gradients, hence the more symmetrical shape of the PDF at small lags. It is not obvious that such large-scale gradients should be removed (see discussion in PF03). The fields mapped here are expected to be small with respect to the integral scale of turbulence L , at least on the order of the molecular cloud size itself. As the lag decreases from $l = 25$ to $l = 3$ pixels, non-Gaussian tails develop. These tails are more pronounced in the Polaris field than in the Taurus one, with CVI values up to 6 times the dispersions $\sigma_{\delta C}$ of the unnormalized PDF (see Table 1). However, since the number of points in Taurus is lower than in the Polaris field, the minimum level of probability reached is an order of magnitude higher (10^{-3} instead of 10^{-4} in Polaris). We also computed the PDF of the increments for the large-scale KOSMA data in the Polaris field (Fig. 6) and we also find increasing non-Gaussian tails as the lag decreases. The dispersions of the PDF are reported in Table 1 and are seen to smoothly connect with the small-scale values computed in the IRAM field.

In both fields, the dependence of $\sigma_{\delta C}$ with l can be well-fitted by a power law $\sigma_{\delta C} \propto l^{0.5}$. The dispersions $\sigma_{\delta C}$ in the Taurus field are a factor ≈ 2 smaller than in the Polaris field. This ratio is also found when comparing the velocity dispersions – either across the plane of the sky (*pos*) or along the line of sight (*los*) – in the two fields (see Table 2). Furthermore, the ratio of the *los* to *pos* dispersions suggests that the depth of the cloud is larger than the extension in the plane of the sky ($los > pos$) (Ossenkopf & Mac Low 2002).

3.2. Non-Gaussianity: the flatness

The deviations of the PDF from a Gaussian shape can be quantified using the flatness (or kurtosis) of a distribution, defined by

$$\mathcal{F}(l) = \frac{\langle \delta C_l^4 \rangle}{\langle \delta C_l^2 \rangle^2} \quad (2)$$

Table 2. Standard deviations σ (in km s^{-1}) of the centroid velocity PDF (*pos*) and of the average line profiles (*los*), computed in three ways in the two fields ($\sigma_1, \sigma_2, \sigma_3$).

Field (1)	Type (2)	Size (3)	σ_1 (4)	σ_2 (5)	σ_3 (6)	$\langle \sigma \rangle$ (7)
Polaris [†]	<i>pos</i>	2.1×2.8	0.54	0.57	0.60	0.57 ± 0.03
	<i>los</i>		1.13	1.10	1.16	1.13 ± 0.03
Polaris [‡]	<i>pos</i>	0.7×0.6	0.31	0.32	0.25	0.29 ± 0.04
	<i>los</i>		0.97	1.02	1.10	1.03 ± 0.05
Taurus [‡]	<i>pos</i>	0.4×0.7	0.12	0.13	0.11	0.12 ± 0.01
	<i>los</i>		0.50	0.60	0.66	0.59 ± 0.07

- (1) For the Polaris field, the IRAM (small) and KOSMA (large) datasets are taken separately. [†]: based on the $^{12}\text{CO}(2-1)$ data, [‡]: $^{12}\text{CO}(1-0)$ data
- (2) the type of PDF (*pos* or *los*)
- (3) Map sizes (in pc \times pc) are computed assuming a distance of 150 pc
- (4) σ_1 is the standard deviation
- (5) σ_2 is derived from a Gaussian fit
- (6) $\sigma_3 = \Delta v_{\text{eq}}/2.35$
- (7) average of the three determinations

where the p th-order moment (for even p) is computed as $\langle \delta C_l^p \rangle = \int \delta C_l^p \mathcal{P}_n(\delta C_l) d(\delta C_l)$. The flatness equals 3 for a Gaussian distribution. The uncertainties, here and for all the moments computed in what follows, are estimated by using two $\mathcal{P}_n(\delta C_l)$ with two thresholds, $N_{\min} = 1$ and 10, and by computing the mean and rms of the two outputs. Fig. 7 displays the flatness of the PDF at all lags, for the two fields. For the Polaris field, the IRAM and KOSMA data have a flatness close to 3 at large lags, which confirms the visual Gaussian shape of the corresponding PDF in Fig. 4. The flatness increases at smaller lags as a result of non-Gaussian tails. For the Taurus field, however, the flatness stays close to 3, confirming that the non-Gaussian tails are less pronounced.

3.3. Structure functions of the line centroid velocities

By analogy with studies performed on the velocity field (*e.g.* She *et al.* 2001), we computed the structure functions of the line CV, using the PDF of the centroid velocity increments $\mathcal{P}_n(\delta C_l)$, a procedure that allows a check of the convergence of the structure functions by filtering out doubtful points in the PDF. The structure functions are evaluated by a direct integration of the PDF:

$$S_p(l) = \int_0^\infty |\delta C_l|^p \mathcal{P}_n(|\delta C_l|) d(|\delta C_l|). \quad (3)$$

Structure functions of velocity are frequently normalized to the third-order function for two reasons: first because in incompressible, isotropic, and homogeneous turbulence, $\zeta(3) = 1$ is an exact result; second because oscillations in $S_p(l) - l$ plots are damped when the S_p are plotted against S_3 , a property called extended self-similarity (ESS) (Benzi *et al.* 1993), so that the range of scales over which the structure functions are power laws is wider.

Calculations of high-order structure functions are susceptible to errors since, as p increases, any spurious large fluctuation largely affects S_p . The calculation of S_p based on Eq. 3 allows us to reject bins populated by too small a number of points, and to study the influence of irrelevant bins of the PDF (for which $N < N_{\min} = 10$). We also applied the procedure described in Lévêque & She (1997) and Padoan *et al.* (2003) for determining the highest significant order: the peak of the histogram of $|\delta C_l|^p$ occurs for a value of δC_l that must be represented by a significant

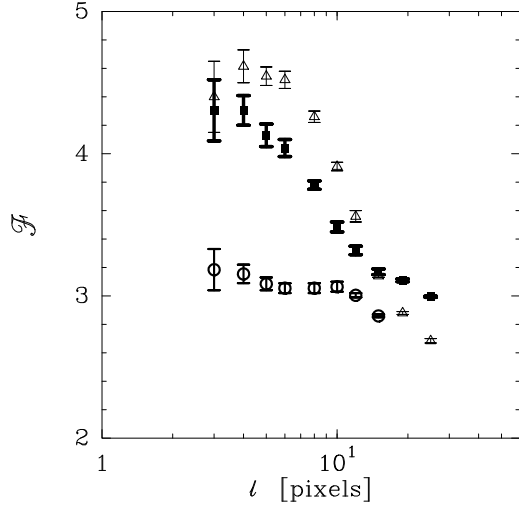


Fig. 7. Flatness \mathcal{F} of the CVI (see Eq. 2) computed from the normalized PDF of CVI. *Squares:* Polaris $^{12}\text{CO}(1-0)$ IRAM data. *Triangles:* $^{12}\text{CO}(2-1)$ KOSMA data. *Circles:* Taurus $^{12}\text{CO}(1-0)$ IRAM data.

number of points in the PDF of δC_l . The maximum significant order found is $p = 6$.

The scalings of S_p with S_3 are shown in Fig. 8 for the Polaris and Taurus fields. They are power laws. Exponents of the structure functions are calculated by fitting the ESS diagrams for lags wider than 2 pixels and smaller than 30 to 60 (see Fig. 8). Error bars on the exponents (1 – 3%) are estimated from weighted averages of the results from two calculations corresponding to $N_{\min}=1$ and 10. The ESS exponent values are given in Table 3. The absolute values of the second-order structure function in the Taurus field are a factor 6 lower than in Polaris, confirming that the Taurus field contains less kinetic energy. The non-ESS fits of the CV structure functions lead to values for $\zeta(3) = 1.35$ and 1.60 in Polaris and Taurus, which differ significantly from the expected value ($\zeta(3) = 1$) for the velocity in incompressible, homogeneous, and isotropic turbulence (Kritsuk et al. 2007).

4. The spatial distribution of the largest line centroid velocity increments

In the following section, we discuss the spatial structures of the largest CVI in the different maps. We compare maps of CVI computed on large and small-scales with large and small beams. For the sake of simplicity, we call shear the CVI value divided by the lag over which it is measured, $\delta C_l/l$. This will be justified at the end of Section 5.

4.1. Locus of the extrema of CVI in the IRAM fields

Figs. 9 and A.3 show the maps of azimuthally averaged CVI ($\langle |\delta C_l| \rangle$) computed for two lags ($l = 3$ and 18 pixels) in both fields. The grey scale is the magnitude of the azimuthally averaged CVI at a given position on the sky. Because of the averaging procedure, the exact values of the CVI in those maps are not trivially related to the values of the non-averaged PDF of Figs. 4 and 5. However, regions of large CVI in the maps do correspond to the positions responsible for the non-Gaussian tails in the PDF of Figs. 4-6.

Table 3. Exponents $\tilde{\zeta}_p = \zeta(p)/\zeta(3)$ of the ESS structure functions of the CV for the Polaris and Taurus fields (see Fig. 14).

	$\tilde{\zeta}_1$	$\tilde{\zeta}_2$	$\tilde{\zeta}_3$	$\tilde{\zeta}_4$	$\tilde{\zeta}_5$	$\tilde{\zeta}_6$
Polaris	0.37	0.70	1.00	1.27	1.53	1.77
Polaris ^(a)	0.38	0.71	1.00	1.28	1.54	1.80
Taurus	0.36	0.69	1.00	1.30	1.60	1.89
SL94 ^(b)	0.36	0.70	1.00	1.28	1.54	1.78
B02 ^(b)	0.42	0.74	1.00	1.21	1.40	1.56

(a) From the large scale $^{12}\text{CO}(2-1)$ data from Bensch et al. (2001).

(b) SL94 and B02 are the She & Lévéque (1994) and Boldyrev et al. (2002) scalings of the velocity structure functions (see Section 5.2).

At a small lag ($l = 3$), in both fields, the spatial distribution of the bright regions with large CVI delineates elongated structures. When the lag is larger (18 pixels), the contrast of the structures above the background values fades away. Yet, in the Polaris field, the structure around $(-1000'', -200'')$ is still visible with $l = 18$, and for the two lags of 3 and 18 pixels, the largest CVI is located in the northwestern corner of the map.

These maps show that the positions of the largest CVI, in Polaris and Taurus, are not randomly distributed but are connected and form elongated structures. In the Taurus field, the direction of the most prominent CVI structure is parallel to the projected orientation of magnetic fields measured in the NE corner of the field (Heiles 2000) (see also Fig. 1). In Polaris, the scatter of their orientations relative to the magnetic field is larger (Paper II). In both Taurus and Polaris, their characteristic half-maximum width, measured on transverse cuts, is resolved ($30''$ after deconvolution from the lag, or $d \approx 0.02$ pc), and their aspect ratio is often greater than 5. The surface fractions covered by the regions where the $\langle |\delta C_l| \rangle$ are larger than $3\sigma_{\text{aver}}$ (where σ_{aver} is the dispersion of the distribution $\langle |\delta C_l| \rangle$), are 10% and 28 % in Polaris and Taurus, respectively. Last, the non-averaged CVI in these structures (see Section 3.1) are 5 and 4 times larger than the dispersion $\sigma_{\delta C}$ (see Figs. 4 and 5) in Polaris and Taurus, respectively. For $l = 3$, the corresponding shears are $5 \times 0.11 \text{ km s}^{-1}/0.02 \text{ pc} = 30 \text{ km s}^{-1} \text{ pc}^{-1}$ in Polaris and $4 \times 0.05 \text{ km s}^{-1}/0.02 \text{ pc} = 10 \text{ km s}^{-1} \text{ pc}^{-1}$ in Taurus. The most turbulent field on the parsec-scale (Polaris) is therefore that where the largest small-scale shears are measured.

4.2. Comparison of the extrema of CVI with the CO emission

We stress here that our work is based on the statistics of the extrema of CVI (called E-CVI in what follows), unlike what is done in most analyses (e.g. Esquivel & Lazarian 2005), where the full distribution of CVI is considered. We show below which specific features of the CO line emission are associated with the extrema of CVI.

Fig. 10 displays two $^{12}\text{CO}(1-0)$ space-velocity cuts made across the Polaris map at longitude offsets $-500''$ and $-800''$. The run of the averaged CV and CVI along these cuts is shown to illustrate that the largest CVI are mostly due to very localized broad CO linewings. As expected, however, some of the large variations in the centroid velocities due to these broad wings are reduced by opposite variations due to fluctuations in the line-core emission.

This is seen better in Fig. 11 where the extrema of centroid velocity increments in the Polaris field are overplotted on the ^{12}CO wing emission and the ^{13}CO integrated emission. The

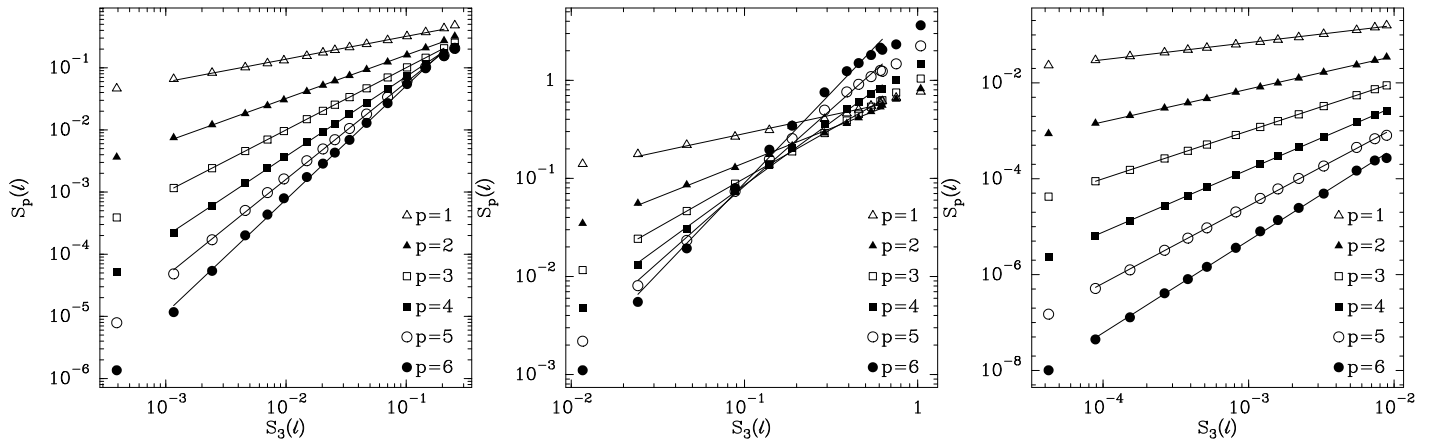


Fig. 8. Structure functions $S_p(l)$ plotted against $S_3(l)$ ($p = 1, \dots, 6$) for Polaris (left for the IRAM data and middle for the KOSMA data) and Taurus (right). A power law is fitted to each order for $l > 2$ pixels, and for $l < 60$, $l < 30$, and $l < 40$ from left to right.

^{12}CO wing emission (top panel) is optically thin and associated with warm and tenuous gas emission (Paper II). The ^{13}CO -integrated emission (bottom panel) is used here as a proxy for the molecular gas column density. While the largest CVI are not spatially correlated with the ^{13}CO -integrated emission, they closely follow the boundaries of the optically-thin ^{12}CO emission in the broad ^{12}CO linewings.

Given the high latitude of the Polaris cloud, the structures responsible for the broad ^{12}CO linewings most likely belong to the Polaris Flare (Fig. 1). The non-Gaussian tails of the PDF at small lags are thus associated to local structures on the scale of 30 pc. Their distance, and therefore their size, is known to within 20%, while the lags of the PDF decrease by an order of magnitude (from 25 to 3). The $l = 3$ pixel PDF is thus sensitive to true small-scale structures created by the turbulence in the Polaris Flare. This comparison shows that the regions of largest shear are not associated with the bulk of the condensed matter in the field, but are instead correlated with warmer and more diluted gas. We therefore infer that, unlike centroid velocities increments in general, the E-CVI we analyze are not due to density fluctuations or radiative transfer effects in optically thick gas.

We now address the issue of the chance coincidence of unrelated pieces of gas on the line of sight. In the two translucent fields, CO is not expected to trace the full molecular content of the clouds, essentially as a result of photodissociation processes. This has possibly been observed by Sakamoto & Sunada (2003) who show discontinuous CO emission in low extinction regions in the Taurus complex. These spots of CO emission are however embedded in the underlying turbulent molecular gas, undetected because mostly made of molecular hydrogen, and presumably continuous. The velocity field deduced from the CO emission lines thus carries the statistical properties of that turbulent molecular gas.

Nonetheless, projection effects are inevitable, and a key parameter is the ratio l/L of the lag l over which CVI are measured to the unknown depth of the cloud along the line-of-sight L . In their work on 512³ numerical simulations of mildly compressible turbulence, Lis et al. (1996) have computed PDF of CVI for a lag of 3 pixels, for which this ratio is $3/512=0.006$. They show that the E-CVI trace extrema of $\langle (\nabla \times \mathbf{v})_y \rangle_{\text{los}}^2 + \langle (\nabla \times \mathbf{v})_z \rangle_{\text{los}}^2$. Since this quantity is a *los* integration of a signed quantity (the two projections of the vorticity in the plane of the sky), its extrema are due to a few exceptional values present on the line of sight. For this reason Lis et al. (1996) say that the E-CVI trace the pro-

jection of large velocity-shears (or vorticity) in turbulence. In Polaris and Taurus, L is not known but we conservatively adopt a value in the range 1 – 30 pc. For the smallest lag ($l = 3$ pixels) the ratio is in the range $l/L = 0.001 - 0.02$. Our observational study thus falls into the regime tested by Lis et al. (1996), and the filaments associated with the E-CVI thus trace the projection of regions of extreme velocity-shear somewhere on the line of sight. The observed value of the shear, though, is of course an upper limit. We are therefore confident that E-CVI trace genuine extrema of line-of-sight velocity fluctuations.

4.3. Parsec-scale coherence of the regions of largest CVI: IRAM and KOSMA data

We compare here the properties of the E-CVI (values and spatial distribution) from the KOSMA and IRAM data sets of the Polaris field. The comparison is not, however, straightforward for two reasons. First, the value of the centroid velocity is affected by the beam size, and second, the computation of the CVI filters out any structures that are much larger than the lag.

Fig. 12 displays the spatial distribution of the CVI computed on large scales with the KOSMA data, for a lag $l = 3$ pixels ($180''$). Regions of large increments are spatially resolved filaments: cuts across the structures provide an average thickness of $200''$ deconvolved from the lag, or 0.18 pc. These structures are about 7 times thicker than those found in the IRAM field. The prominent KOSMA structure around $(123.29^\circ, 25.11^\circ)$ smoothly connects with the northwestern IRAM structure (contours from Fig. 11). This is seen more clearly in Fig. 13 where the values of the non-averaged CVI along this structure are displayed. Fig. 13 illustrates three points: *i*) the CVI from the KOSMA and IRAM datasets decrease monotonously from north to south along this structure, *ii*) the IRAM CVI measured over $l = 180''$ are all larger than those measured with KOSMA over the same physical lag, and *iii*) the CVI measured with the KOSMA telescope over a lag of 3 pixels ($180''$) are similar to those measured at the same positions with the IRAM telescope with a lag 6 times smaller ($30''$) and .

The latter property is unexpected: it suggests that the CVI are similar in this region whether they are measured with a small beam and a small lag (IRAM) or a large beam and a large physical lag. If the KOSMA structures were only due to beam-dilution of the IRAM ones, the KOSMA CVI for $l = 180''$ would be

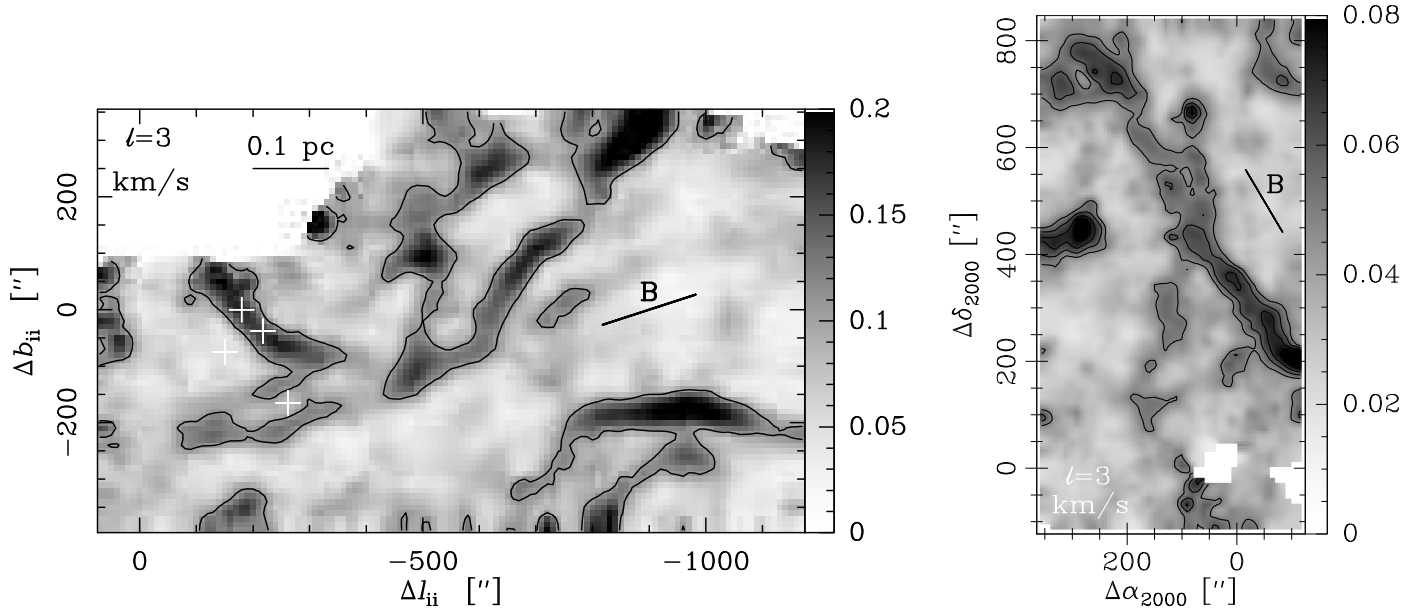


Fig. 9. Spatial distribution of the azimuthally averaged CVI (*i.e.* $\langle |\delta C_l| \rangle$) computed with lags $l = 3$ based on the $^{12}\text{CO}(1-0)$ line. The grey-scale gives the $\langle |\delta C_l| \rangle$ in km s^{-1} . The dark regions correspond to large values of the CVI associated to the tails of the $\mathcal{P}(\delta C_l)$ (Fig. 4 and 5). The orientations of the magnetic fields (Heiles 2000) are also shown. *Left panel:* Polaris field. Contours indicate the 0.11 and 0.22 km s^{-1} levels. The largest CVI (0.30 km s^{-1}) appear in the NW corner of the field. The 4 crosses indicate the positions where the HCO^+ abundances have been measured (Paper I). *Right panel:* Taurus field. Map center is $\alpha_{2000} = 04^{\text{h}}40^{\text{m}}08.84^{\text{s}}$, $\delta_{2000} = 24^{\circ}12'48.40''$. Offsets are in $''$. Contours: 0.05 km s^{-1} with 0.01 km s^{-1} steps. Note that the largest CVI (0.10 km s^{-1}) in that field are 3 times smaller than in the Polaris field. The blanked areas around (0, 0) offsets correspond to the positions where the 10 km s^{-1} component is present.

smaller than the IRAM ones for $l = 30''$. In other words, the KOSMA CVI structures are real and are sub-structured: the same velocity variations ($< 0.5 \text{ km s}^{-1}$ for positive offsets) are measured on small (IRAM) and large (KOSMA) scales.

The largest velocity-shears at the KOSMA resolution are $5 \times 0.30 / 0.18 \approx 8.3 \text{ km s}^{-1} \text{ pc}^{-1}$. The surface fraction covered by the large increment structures where $\langle |\delta C_l| \rangle > 3\sigma_{\text{aver}}$ are close, 10 and 16% for the IRAM and KOSMA data, respectively. These two fields, observed with different telescopes and resolutions, thus show similar statistical properties and demonstrate the coherence at the parsec-scale of the structures of largest centroid velocity increments. This is discussed in the next section.

5. The two facets of intermittency: statistical and structural

In Section 3, the two-point statistics of the line centroid velocities were found to display marked non-Gaussian behaviors. In Section 4, the emission responsible for these non-Gaussian statistics is resolved into coherent structures. We here compare these statistical and structural characteristics with theoretical predictions and recent numerical results regarding the intermittency of turbulence.

5.1. Self-similarity of the centroid velocity increments in the Polaris field

The IRAM and KOSMA PDF from Figs. 4 and 6 bear an apparent contradiction: the PDF built with the IRAM data with a lag of $150''$ (15 pixels) is nearly Gaussian, while the KOSMA PDF with a similar physical lag of $180''$ (3 pixels) is not: non-Gaussian tails

in the KOSMA PDF originate from the largest CVI structures like the most prominent one discussed in Section 4.3. In Fig. 13, we show that the bulk of the IRAM CVI for $l = 180''$ (dark dots) are below $3\sigma_{\delta C} = 0.9 \text{ km s}^{-1}$. It is the particular location of the IRAM field with respect to the CVI maxima seen in the KOSMA field that prevents the detection of a number of CVI in excess of $3\sigma_{\delta C}$ large enough to depart from Gaussian statistics. Would the IRAM field be centered closer to the CVI maximum in the KOSMA data (around $123.29^\circ, 25.11^\circ$), a larger number of CVI in excess of $3\sigma_{\delta C}$ might have been measured.

However, in both fields, the non-Gaussian tails of the PDF of CVI grow as the lag decreases. This behavior is routinely observed in laboratory and numerical experiments, where it is interpreted as a signature of the intermittency of the velocity field. In such experiments, effects of the non-Gaussian statistics are visible with either the transverse or the longitudinal velocity increments (Frisch 1995; Mininni *et al.* 2006a). The present analysis shows various degrees of non-Gaussianity: the statistics in Taurus are nearly Gaussian (flatness close to 3), while both Polaris data sets show clear departure from Gaussianity. If, following PF03, we attribute the non-Gaussian statistics of the CVI to the intermittency of the turbulence in the two sampled molecular clouds (see below), the new result, here, is that intermittency is as pronounced at a lag $l = 180''$ in the large field (KOSMA PDF) as it is at lag $l = 30''$ in the IRAM field. In both datasets, the non-Gaussian tails extend to $5.5 - 6\sigma_{\delta C}$. This suggests that intermittency is not only a small-scale phenomenon but that it is present and has the same statistical properties on a scale six times larger.

As mentioned in the introduction, similar conclusions have been reached by MJ04, who find that the intense structures of vorticity and rate of strain in hydrodynamical turbulence form

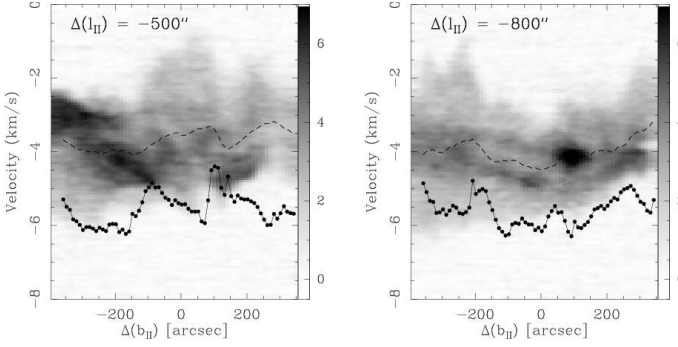


Fig. 10. Position-velocity cuts at constant ℓ_{II} offsets ($\Delta\ell_{\text{II}} = -500''$, left and $\Delta\ell_{\text{II}} = -800''$, right). *Grey-scale*: main-beam intensity in K. *Dashed curve*: centroid velocity. *Full curve*: azimuthally averaged CVI for a lag $l = 3$ pixels (with an additional offset of -6.5 km s^{-1} for clarity).

clusters of inertial range extent, implying a large-scale organization of the small-scale intermittent structures.

5.2. The intensity of small-scale intermittency versus large-scale shear

We now compare the scaling of the p^{th} -order structure functions of CV with p in the framework of the SL94 model. Structure functions are increasingly sensitive to the tails of the CVI PDF (E-CVI) as the order p increases. Since we have shown (Sect 4.2) that the E-CVI stem from velocity fluctuations, it is interesting to compare the scaling of high order structure functions of the CV to theoretical predictions based on the velocity field.

The SL94 model has three parameters (see Appendix A.3). One of the three parameters, $0 \leq \beta \leq 1$, describes the level of intermittency: $\beta \rightarrow 1$ corresponds to the non-intermittent cascade with $\tilde{\zeta}_p = p/3$. The two other parameters (Boldyrev et al. 2002) describe the scalings of velocity in the cascade and the dimension D of the most intermittent structures. In the SL94 model, the scaling of the velocity is $v_l \sim l^{1/3}$. It assumes that the most intermittent structures are filaments ($D = 1$) and that the level of intermittency is $\beta = 2/3$. The associated ESS structure function exponents $\tilde{\zeta}_p = \zeta(p)/\zeta(3)$ are then predicted to be $\tilde{\zeta}_p^{\text{SL}} = p/9 + 2[1 - (2/3)^{p/3}]$. According to this class of models, as the level of intermittency increases, the ESS exponents become smaller than $p/3$ for $p > 3$ and the departure from the K41 scaling increases with p . Following the SL94 approach, further theoretical models were developed for compressible and magnetized turbulence (Politano & Pouquet 1995; Müller & Biskamp 2000) and tested against numerical simulations. Boldyrev et al. (2002) propose a similar scaling to describe compressible MHD turbulence assuming sheet-like intermittent structures ($D = 2$) and a more intermittent cascade ($\beta = 1/3$) but do not allow dissipation of large-scale modes in shocks. They find $\tilde{\zeta}_p^{\text{B02}} = p/9 + 1 - (1/3)^{p/3}$ (hereafter called the B02 scaling), in excellent agreement with numerical simulations of super-Alfvénic MHD turbulence. However, this scaling has never been tested against observations of the turbulent velocity field of molecular clouds.

In Fig. 14, we compare the scalings of the CV structure functions exponents (see Table 3) with the predictions of the SL94 and B02 models for the velocity field. In the Polaris field, for either data set, the measured exponents follow the SL94 scaling closely but differ significantly from that of B02. This apparent agreement with the SL94 scaling is unexpected since this model

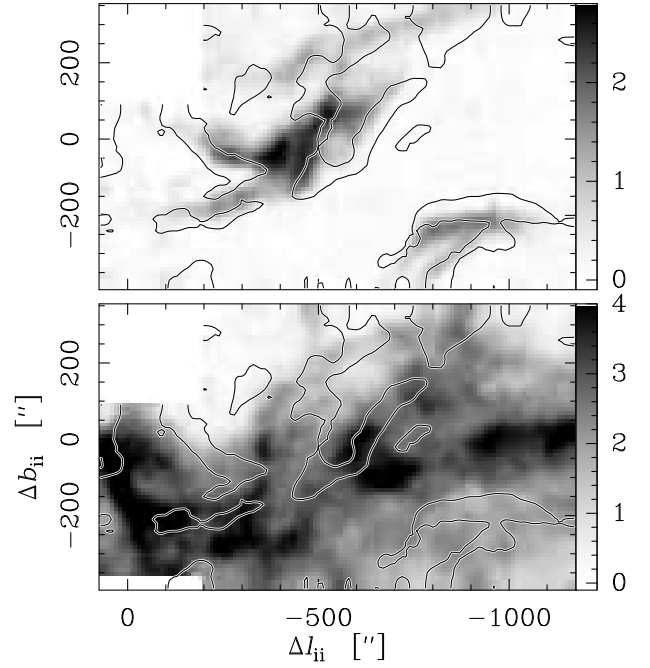


Fig. 11. Contours of the CVI (1 km s^{-1}) computed in the Polaris field for $l = 3$ pixels (see Fig. 9) overplotted on the $^{12}\text{CO}(1-0)$ emission integrated in the velocity range $[-2, 5 : 0] \text{ km s}^{-1}$ i.e. optically thin ^{12}CO emission (top) and the ^{13}CO integrated intensity tracing the bulk of the dense gas (see Paper II) (bottom).

describes incompressible and unmagnetized turbulence, everything interstellar turbulence is not. However, the effect of line-of-sight averaging in the CV structure functions is not known. Further interpretation of the underlying physics requires confrontation with CV structure functions based on numerical simulations. The exponents in the Taurus field do not follow any of the three scalings, and are halfway between the non-intermittent K41 scaling ($\tilde{\zeta}(p) = p/3$) and the SL94 scaling. The Taurus field is thus less intermittent than the Polaris one, a result consistent with the flatness measure of the non-Gaussianity of the $\mathcal{P}(\delta C_l)$. This result is also in line with the recent numerical findings of Mininni et al. (2006a), who show that the characteristics of the large-scale flow play an important role in the development of small-scale intermittency and determine its statistical properties.

The use of CV structure functions to determine the three parameters of the SL94 class of models not only requires a large number of data points but also “calibration” of the weighting performed by CV upon the velocity field, using numerical simulations of compressible turbulence. The values that we have determined from the exponents $\tilde{\zeta}(p)$ may be useful, though, and we give them in the Appendix.

In summary, the line CV exhibit the statistical and structural properties characterizing the intermittency of the velocity field in theoretical models and numerical simulations of turbulence: 1) the non-Gaussian statistics of the CVI at small lag, 2) the self-similarity of structures of largest CVI and the existence of inertial-range intermittency, 3) the anomalous scaling of their high-order structure functions similar to what is found for the structure functions of velocity. Last, we find that the more intermittent field on small scales has the larger dispersion of non-thermal velocity on large scales.

The above properties are borne by the non-Gaussian tail of the CVI PDF, which we have shown to be associated with pure

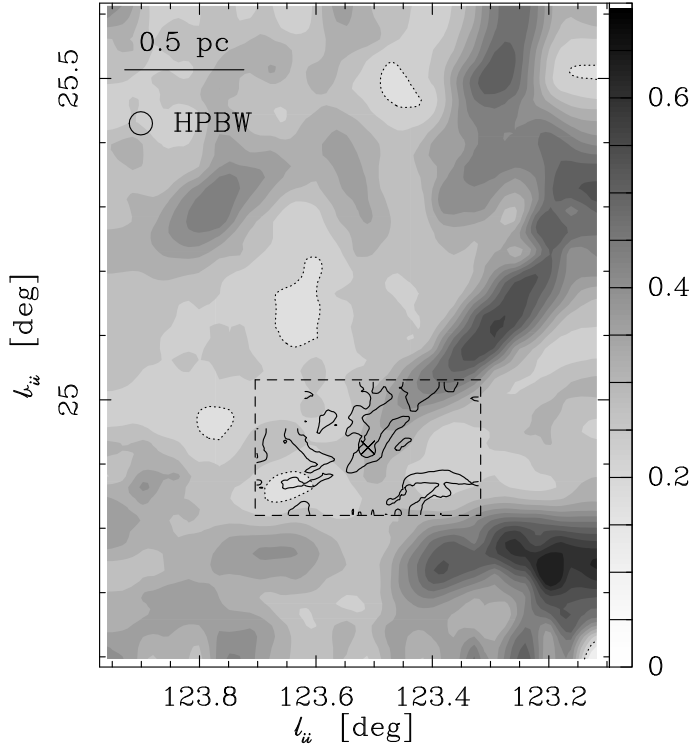


Fig. 12. Spatial distribution of CVI (km s^{-1}) computed on large scales using the data of Bensch et al. (2001) (grey-scale with levels indicated on the right scale, dotted contours indicate the 0.1 km s^{-1} level). Full-line contours indicate the CVI computed on small scales in the IRAM-30m data cube (see Fig. 11). Note the spatial coincidence of the IRAM structures at the tip of the prominent KOSMA structure at $(123.4^\circ, 25^\circ)$, where the CVI are 0.30 km s^{-1} .

velocity fluctuations. They support our proposition that statistics of the ^{12}CO line centroid velocity and, more specifically, their E-CVI may be used to disclose the statistical and structural properties of intermittency in the underlying velocity field. In what follows, we therefore ascribe the E-CVI to the intermittent structures of intense shears.

6. Discussion

6.1. Influence of gravity

To test the role of gravity in the generation of non-Gaussian statistics of the velocity, Klessen (2000) built the two-point statistics of the velocity field, in SPH numerical simulations of turbulence, both with and without self-gravity. The author compared the numerical PDF of CVI with observed PDF and concluded that the inclusion of self-gravity leads to better agreement with the observed PDF in molecular clouds. It was further argued in PF03 that this result was indeed expected since the observed regions used in the comparison are forming stars, hence the importance of self-gravity. The situation is drastically changed in the two translucent fields we have studied: they do not form stars, are far from any such regions, and both are non-self-gravitating on the parsec-scale of our observations. Indeed, we have shown that the field with the more prominent non-Gaussian tails, namely Polaris, is located at high latitude and is embedded in a larger structure (the Flare) far from virial bal-

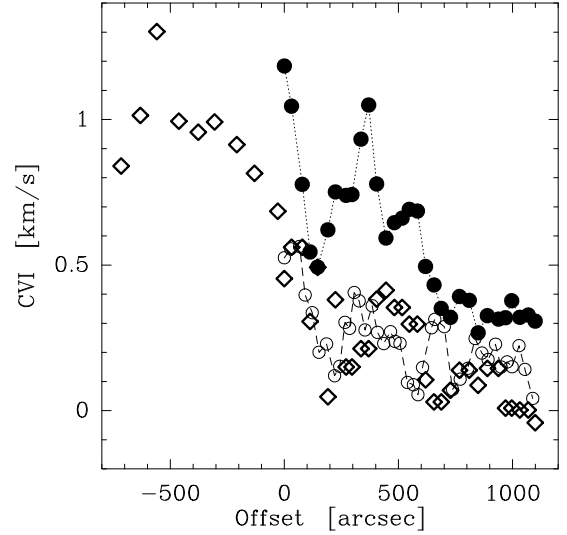


Fig. 13. Values of the CVI in the Polaris field, along the NW-SE CVI structure from $(123.2, 25.2^\circ)$ to $(123.6, 24.9^\circ)$ seen in Fig. 12. CVI are from KOSMA data for $l = 3$ (diamonds), IRAM $l = 3$ (open circles), and IRAM $l = 18$ (filled circles). Offsets increase from NW to SE, with the zero position corresponding to the NW corner of the IRAM field (see Fig. A.2).

ance. This strongly supports that, in the type of fields we analyze, gravity is not at the origin of the PDF tails.

Nonetheless, gravity is the ultimate source of gas motions in the universe, from galaxy clusters to GMC and collapsing cores, so it cannot be ignored. If the cloud mass were distributed in tiny cloudlets of very high density that would rarely collide, then gravity might play a significant role in the gas velocity statistics. Here, we assume that the fluid approximation is valid, and because the Reynolds number is so large, the gas motions are turbulent, by definition.

6.2. The intermittency of turbulence dissipation

In numerical experiments such as those of MJ04 (see also Sreenivasan 1999), maxima of energy dissipation are found, at small-scale, in the vicinity of the vorticity filaments. A large fraction of the dissipation of turbulence may be concentrated in the regions of largest CVI, the small-scale intermittent structures. We illustrate this point with estimates of energy transfer based on our observations in the Polaris field.

The transfer rate in the cascade on scale l is $\epsilon_l = 1/2\rho\bar{v}_l^3/l$ with \bar{v}_l the characteristic turbulent velocity fluctuations on that scale. This assumes that the time to transfer energy from scale l to smaller scales writes as $\tau_l = l/\bar{v}_l$. At the parsec-scale of the Polaris cloud

$$\epsilon_L = 5.5 \times 10^{-25} / L_{\text{pc}}^2 \quad \text{erg s}^{-1} \text{ cm}^{-3} \quad (4)$$

where the average density $\rho = \mu N_H / L$ and the velocity dispersion $\bar{v}_L = 1.5 \text{ km s}^{-1}$ are those derived in Paper II. There, L_{pc} is the unknown depth along the line of sight, expressed in pc. The CO cooling rate averaged over the whole field on the parsec-scale is (Paper II)

$$\bar{\Lambda}_{\text{CO}} = 10^{-24} / L_{\text{pc}} \quad \text{erg s}^{-1} \text{ cm}^{-3}. \quad (5)$$

These two rates are thus close, because the depth along the line of sight is not much greater than 1 pc (see Section 3.1),

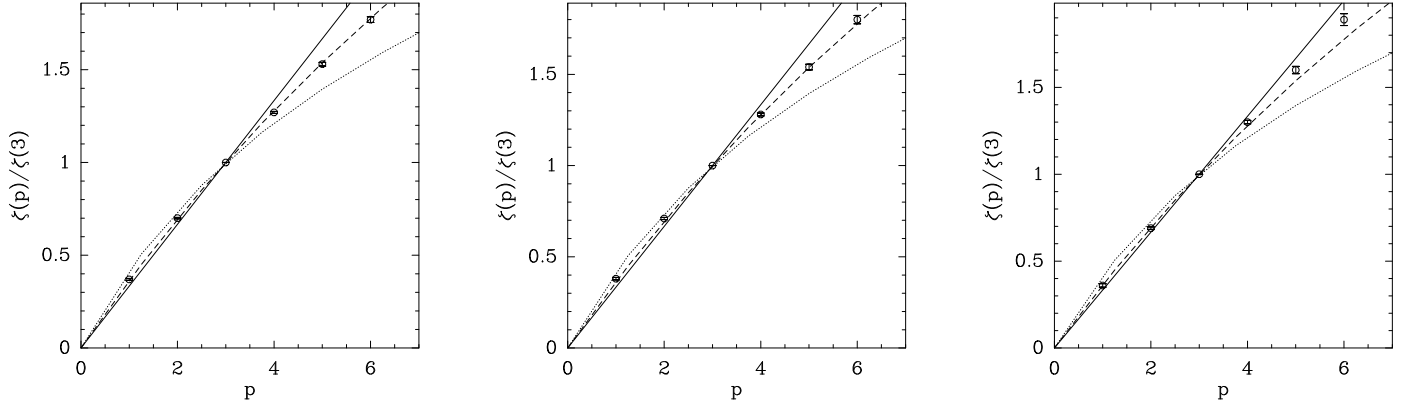


Fig. 14. Values of the exponents of the structure functions (see Fig. 8) with error bars (see Table 3). For comparison, the K41 (full), SL94 (dashed), and B02 (dotted) scalings are indicated. From left to right: Polaris (IRAM), Polaris (KOSMA), Taurus.

and may lead to the conclusion that CO is able to radiate the turbulent energy away, confirming the results of Shore et al. (2006). Actually, this would be true if the cascade were filling space uniformly or, in other words, for a non-intermittent cascade. From the previous section, this assumption is certainly not valid. Indeed, the cumulative distribution of δC_l^2 for $l = 3$ (see Fig. B.1) shows that the points with CVI larger than $3\sigma_{\delta C}$ represent only 2.5% of the total, while they contribute to 25% of the total of δC_l^2 . The velocity field has two contributions (solenoidal and dilatational) to the energy dissipation rate $\epsilon = -\frac{1}{\text{Re}}(|\nabla \times \mathbf{v}|^2 + \frac{4}{3}|\nabla \cdot \mathbf{v}|^2)$ (Kritsuk et al. 2007). As shown by Lis et al. (1996) and Pety & Falgarone (2000) based on numerical simulations, the E-CVI serve as a proxy for large vorticity regions. Thus, assuming that the energy dissipation on scale l is proportional to δC_l^2 , the cumulative distribution of Fig. B.1 suggests that the local dissipation rate at $l = 3$ (or ~ 0.02 pc) in the E-CVI regions, is already 10 times larger than the average rate over the field, $\epsilon_{\text{E-CVI}} > 10\epsilon_L$. Note that these numbers are about the same for the large-scale Polaris field, while in the less intermittent Taurus field, these E-CVI represent only 1% of the total, still contributing to 5% of the dissipation.

On the actual dissipation scale, presumably smaller than 0.02 pc, the local dissipation rate is still higher by an unknown factor. Since the turbulent dissipation is not space-filling, it induces high local heating rates. This suggests that other cooling agents, *e.g.* the pure rotational lines of H_2 or the fine structure line of C^+ , may be dominating the cooling in these regions (Paper I and Falgarone et al. 2007). Observations are still lacking that would allow a comparison of the turbulent transfer rate with the CO cooling rate on scales smaller than 0.02 pc.

In spite of the self-similarity of the intermittent structures discussed in Section 5, the bulk of the dissipation is likely to take place in the smallest structures. The largest CVI are proportional to $\sigma_{\delta C}$ and thus to $l^{1/2}$. The corresponding shears therefore scale as $l^{-1/2}$ providing an observed scaling of the dissipation rate with lengthscale l , $\epsilon_l \propto l^{-1}$. Now, we use the finding of MJ04, who show that the tails of the probability distribution functions of the volume of individual dissipative structures (either intense vorticity or strain-rate) decrease approximately as $p(V) \sim V^{-2}$. Whether these structures are cylinders ($V \propto l^2$) or sheets ($V \propto l$), the integrated dissipation is therefore always dominated by the dissipation which takes place on the smallest scales, because $p(V)\epsilon_l \propto l^{-5}$ in the first case or $\propto l^{-3}$ in the second case.

This confirms the important point for the evolution of molecular clouds that dissipation of turbulence is concentrated in a small subset of space. The induced radiative cooling, and therefore the dissipation rate, have to be searched on scales on the order of the milliparsec in emission lines more powerful than the low- J CO transitions. The value of the rate itself may thus be directly observable in line emissions (pure rotational lines of H_2 , C^+) that can only be distinguished from UV-excited emission by observations at very high angular resolution.

7. Conclusion and perspectives

We performed a statistical analysis of the turbulence towards two translucent molecular clouds based on the two-point probability density functions of the $^{12}\text{CO}(1-0)$ line centroid velocity.

Thanks to the excellent quality of the data, we prove the non-Gaussian tails in the PDF of the line centroid velocity increments on small-scales, down to a probability level of 10^{-4} . We show that the largest CVI, in both fields, delineate elongated narrow structures (~ 0.02 pc) that are, in one case, parallel to the local direction of the magnetic field. In the Polaris field, these filaments are well-correlated to the warm gas traced by the optically thin $^{12}\text{CO}(1-0)$, while they do not follow the distribution of matter traced by the ^{13}CO . Using large-scale data, we have shown that these filamentary structures remain coherent over more than a parsec. Furthermore, the similar statistics found in the IRAM and KOSMA maps of this field suggest that both samples belong to the self-similar turbulent cascade. In the Polaris field, the high-order structure function exponents, computed up to order $p = 6$, significantly depart from their Kolmogorov value.

Through the properties of the tails of their PDF, *i.e.* the E-CVI, the line centroid velocities in these two clouds are found to carry the main signatures of intermittency borne by a turbulent velocity field. The departure from the Gaussian statistics of the centroid velocity increments on small-scales is therefore ascribed to the intermittency of turbulence, *i.e.* the non-space filling character of the turbulent cascade. The structures of largest CVI trace the intermittent structures of intense shears and the sites of intermittent turbulence dissipation. We show that these intermittent structures, on the 0.02 pc-scale, harbour 25% and 5% of the total energy dissipation, in the Polaris and Taurus fields, respectively, although they fill less than 2.5% and 1% of the cloud area. We find that both fields are intermittent and that the more intermittent velocity field on small scales (the Polaris field) belongs to a molecular cloud far from virial balance on

the scale of 30 pc. In contrast, the less intermittent (the Taurus field) belongs to a virialized complex. The more turbulent field is thus the more intermittent. Interestingly enough, the less turbulent field is embedded in a star-forming cloud (Taurus complex) with numerous young stellar objects, while the more turbulent (Polaris) is in an inactive complex.

The exact nature of these intermittent structures, their link with shocks, and the role of magnetic fields are still elusive. The comparison of observational data with theoretical scalings requires the ability to compute higher orders of the structure functions and establish the correspondence between the centroid velocity and the velocity fields. This stresses the need for large homogeneous data samples with at least 10^5 spectra. Such data sets would also allow determination of the three parameters of the class of models to which the SL94 or MHD scalings belong.

Heterodyne instrumentation (*e.g.* multi-beam receiver heterodyne arrays) offers a dramatic increase in the spatial dynamical range accessible, combining high spatial and spectral resolutions. Sub-arcsecond resolution is needed to resolve the dissipation scale, combined with a large instantaneous field of view to disclose the shape of the dissipative structures. Observational signatures of the dissipation of the turbulent kinetic energy might be searched for in chemical abundances of species, whose formation requires high temperatures (Paper I), like CH^+ , HCO^+ , and water. Excited H_2 was also proposed as a good coolant candidate (Falgarone *et al.* 2005; Appleton *et al.* 2006). While some of these observational requirements are already met by existing instruments (*e.g.* HERA at the IRAM-30m telescope), ALMA, SOFIA, and the Herschel satellite will definitely open new perspectives in this field.

Acknowledgements. We thank the anonymous referee for his careful reading of the manuscript and useful comments that helped us to improve the paper. EF and PHB acknowledge the hospitality of the Kavli Institute for Theoretical Physics (Grant No. PHY05-51164) during the revision phase of their manuscript. The authors also thank A. Lazarian for useful comments and M.-A. Miville-Deschênes for providing them with the IRIS maps of Fig. 1.

References

- Abergel, A., Boulanger, F., Fukui, Y., & Mizuno, A. 1995, *A&AS*, 111, 483
 Anselmet, F., Antonia, R. A., & Danaila, L. 2001, *Planet. Space Sci.*, 49, 1177
 Anselmet, F., Gagne, Y., Hopfinger, E. J., & Antonia, R. A. 1984, *J. Fluid Mech.*, 140, 63
 Appleton, P. N., Xu, K. C., Reach, W., *et al.* 2006, *ApJ*, 639, L51
 Bate, M. R., Bonnell, I. A., & Bromm, V. 2002, *MNRAS*, 332, L65
 Bensch, F., Stutzki, J., & Ossenkopf, V. 2001, *A&A*, 366, 636
 Benzi, R., Ciliberto, S., Tripiccone, R., *et al.* 1993, *Phys. Rev. D*, 48, 29
 Boldyrev, S., Nordlund, Å., & Padoan, P. 2002, *Phys. Rev. L.*, 89, 031102
 Bruno, R. & Carbone, V. 2005, *Living Rev. Solar Phys.*, 2
 Cambrésy, L. 1999, *A&A*, 345, 965
 Cambrésy, L., Boulanger, F., Lagache, G., & Stepnik, B. 2001, *A&A*, 375, 999
 Ciolek, G. E. & Basu, S. 2006, *ApJ*, 652, 442
 Crutcher, R. M. 1999, *ApJ*, 520, 706
 Crutcher, R. M. 2005, in *AIP Conf. Proc. 784: Magnetic Fields in the Universe: From Laboratory and Stars to Primordial Structures.*, ed. E. M. de Gouveia dal Pino, G. Lugones, & A. Lazarian, 129–139
 Douady, S., Couder, Y., & Brachet, M. E. 1991, *Phys. Rev. L.*, 67, 983
 Elmegreen, B. G. & Scalo, J. 2004, *Annual Review of Astronomy and Astrophysics*, 42, 211
 Esquivel, A. & Lazarian, A. 2005, *ApJ*, 631, 320
 Falgarone, E., Hily-Blant, P., Pety, J., & Pineau Des Forêts, G. 2007, in *IAU Symposium, Vol. 237, IAU Symposium*, ed. B. G. Elmegreen & J. Palous, 24–30
 Falgarone, E., Panis, J.-F., Heithausen, A., *et al.* 1998, *A&A*, 331, 669
 Falgarone, E., Pety, J., & Hily-Blant, P. 2008, *in prep.*
 Falgarone, E., Pineau Des Forêts, G., Hily-Blant, P., & Schilke, P. 2006, *A&A*, 452, 511
 Falgarone, E., Verstraete, L., Pineau Des Forêts, G., & Hily-Blant, P. 2005, *A&A*, 433, 997

- Frisch, U. 1995, *Turbulence. The legacy of A.N. Kolmogorov* (Cambridge University Press)
 Gerin, M., Falgarone, E., Joulain, K., *et al.* 1997, *A&A*, 318, 579
 Heiles, C. 2000, *Astron.J.*, 119, 923
 Heithausen, A. 2002, *A&A*, 393, L41
 Heithausen, A. & Thaddeus, P. 1990, *ApJ*, 353, L49
 Hily-Blant, P. & Falgarone, E. 2007a, *A&A*, 469, 173
 Hily-Blant, P. & Falgarone, E. 2008, *in prep.*
 Hily-Blant, P., Pety, J., & Falgarone, E. 2007b, in *Astronomical Society of the Pacific Conference Series, Vol. 365, SINS - Small Ionized and Neutral Structures in the Diffuse Interstellar Medium*, ed. M. Haverkorn & W. M. Goss, 184–+
 Klessen, R. S. 2000, *ApJ*, 535, 869
 Klessen, R. S. 2001, *ApJ*, 556, 837
 Kritsuk, A. G., Norman, M. L., Padoan, P., & Wagner, R. 2007, *ApJ*, 665, 416
 Lazarian, A. & Pogosyan, D. 2000, *ApJ*, 537, 720
 Lesieur, M. 1997, *Fluid Mechanics and its Applications, Vol. 40, Turbulence in Fluids*, 3rd edn. (Dordrecht, Netherlands: Kluwer)
 Lévêque, E. & She, Z.-S. 1997, *Phys. Rev. D*, 55, 2789
 Levrier, F. 2004, *A&A*, 421, 387
 Lis, D. C., Keene, J., Li, Y., Phillips, T. G., & Pety, J. 1998, *ApJ*, 504, 889
 Lis, D. C., Pety, J., Phillips, T. G., & Falgarone, E. 1996, *ApJ*, 463, 623
 Mac Low, M. & Klessen, R. S. 2004, *Rev. Mod. Phys.*, 76, 125
 Matthews, B. C. & Wilson, C. D. 2000, *ApJ*, 531, 868
 Mininni, P. D., Alexakis, A., & Pouquet, A. 2006a, *Phys. Rev. D*, 74, 016303
 Mininni, P. D., Pouquet, A. G., & Montgomery, D. C. 2006b, *Phys. Rev. L.*, 97, 244503
 Miville-Deschênes, M.-A., Levrier, F., & Falgarone, E. 2003, *ApJ*, 593, 831
 Miville-Deschênes, M.-A. & Lagache, G. 2005, *Ap. J. Supp.*, 157, 302
 Moisy, F. & Jiménez, J. 2004, *J. Fluid Mech.*, 513, 111
 Müller, W.-C. & Biskamp, D. 2000, *Phys. Rev. L.*, 84, 475
 Ossenkopf, V., Esquivel, A., Lazarian, A., & Stutzki, J. 2006, *A&A*, 452, 223
 Ossenkopf, V. & Mac Low, M.-M. 2002, *A&A*, 390, 307
 Padoan, P., Boldyrev, S., Langer, W., & Nordlund, Å. 2003, *ApJ*, 583, 308
 Padoan, P., Juvela, M., Goodman, A. A., & Nordlund, Å. 2001, *ApJ*, 553, 227
 Pety, J. & Falgarone, E. 2000, *A&A*, 356, 279
 Pety, J. & Falgarone, E. 2003, *A&A*, 412, 417
 Politano, H. & Pouquet, A. 1995, *Phys. Rev. D*, 52, 636
 Porter, D. H., Pouquet, A., & Woodward, P. R. 1994, *Phys. Fluids*, 6, 2133
 Rosolowsky, E. W., Goodman, A. A., Wilner, D. J., & Williams, J. P. 1999, *ApJ*, 524, 887
 Sakamoto, S. & Sunada, K. 2003, *ApJ*, 594, 340
 She, Z.-S. & Lévêque, E. 1994, *Phys. Rev. L.*, 72, 336
 She, Z.-S., Ren, K., Lewis, G. S., & Swinney, H. L. 2001, *Phys. Rev. D*, 64, 016308
 Shore, S. N., Larosa, T. N., Chastain, R. J., & Magnani, L. 2006, *A&A*, 457, 197
 Sreenivasan, K. R. 1999, *Rev. Mod. Phys.*, 71, S383
 Tassis, K. & Mouschovias, T. C. 2004, *ApJ*, 616, 283
 Ungerechts, H. & Thaddeus, P. 1987, *Ap. J. Supp.*, 63, 645
 Vincent, A. & Meneguzzi, M. 1991, *J. Fluid Mech.*, 225, 1

Appendix A: Two-point statistics

A.1. Construction of the $\mathcal{P}_n(\delta C_l)$

In each PDF, all the bins which are associated to a number of events less than a given value N_{\min} , are blanked. The value of N_{\min} depends on the number of bins in the histogram. In Fig. A.1, we show the $\mathcal{P}_n(\delta C_l)$ computed for $l = 3$ in the Polaris field, for successive values of $N_{\min}=0, 10, 30$, and 100. It is seen that, with $N_{\min}=10$, the spurious bins having a constant value $\approx 10^{-4}$ are eliminated. The value of each bin and its uncertainty are then determined from the average and rms of all the points populating the bin.

A.2. CVI maps

The non-averaged CVI map of Fig. A.2, computed in the IRAM data for a lag of 18 pixels (or $180''$), shows that large-scale structures exist that are not filtered out with large enough lags. The crosses indicate the positions where the CVI values of Fig. 13 have been taken.

Figure A.3 shows the CVI map computed in the IRAM Polaris and Taurus fields, for a lag of 18 pixels. The comparison with the CVI maps of Fig. 9 shows that the thin filaments have faded away. However, in the Polaris map, the structure visible at a lag of 3 pixels is still visible, though it has broadened.

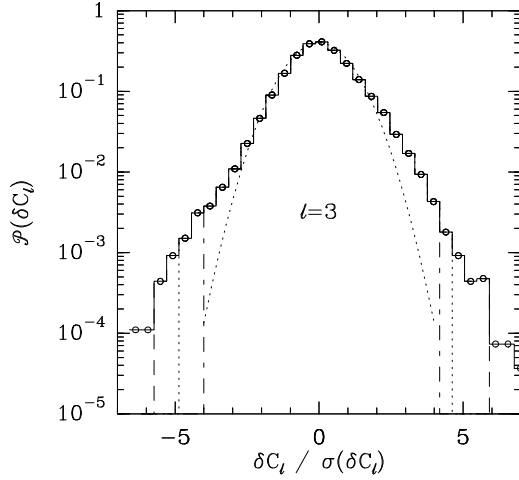


Fig. A.1. $\mathcal{P}_n(\delta C_l)$ computed for $l = 3$ in the Polaris field, for successive values of $N_{\min}=0, 10$ (dashed), 30 (dotted), and 100 (dot-dashed).

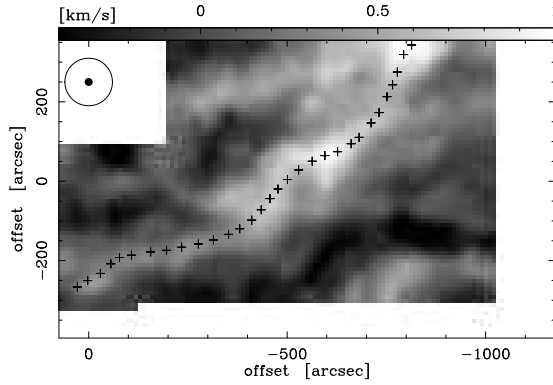


Fig. A.2. CVI map computed from the IRAM dataset with a lag $l = 18$ pixels (or $180''$). CVI are in km s^{-1} . The crosses indicate the positions used for the cut of Fig. 13. The KOSMA and IRAM beams are indicated in the top left corner.

A.3. Determination of the intermittency level

She & L  v  que (1994) developed a model to analyze the small-scale properties of an incompressible turbulent flow. Since this model inspired numerous works of astrophysical relevance, we summarize its key points here. SL94 propose studying the large fluctuations of ϵ_l (defined as the dissipation rate averaged over balls of size l) through the ratio of its successive moments $\epsilon_l^{(p)} = \langle \epsilon_l^{p+1} \rangle / \langle \epsilon_l^p \rangle$. Hence, for each p , the value of $\epsilon_l^{(p)}$ describes the dissipation intensity of a set of turbulent structures: as p increases, the associated structures are more coherent and more singular. As a result, the hierarchical structures of the SL94 model are not related to any physical objects, except for the most intermittent. The SL94 model has three parameters: the scaling of the velocity with scale l , assumed to be that of the K41 theory ($\bar{v}_l \sim l^{1/3}$); the level of intermittency characterized by a parameter β ; and the dimensionality D of the most intermittent structures. Assuming $\beta = 2/3$ and $D = 1$, SL94 proposed a recursive relation linking $\epsilon_l^{(p+1)}$ to $\epsilon_l^{(p)}$,

$$\epsilon_l^{(p+1)} = A_p \epsilon_l^{(p)\beta} \epsilon_l^{(\infty)1-\beta}, \quad (\text{A.1})$$

which allowed them to compute the anomalous scaling of the energy dissipation rate with scale l , $\langle \epsilon_l^p \rangle \sim l^{\tau_p}$, with $\tau_p = -2/3p + 2[1 - (\frac{2}{3})^p]$.

In principle, by fitting the exponents $\tilde{\zeta}(p)$, it should be possible to determine the three parameters of the SL94 class of models. In practice, a reliable determination of the three parameters, *e.g.* by least-square fitting the exponent values, requires computing high-order structure functions ($p > 6$). With 6 orders, we could only determine one parameter, the scaling of the velocity fluctuations in the cascade $\bar{v}_l \propto l^\theta$ and we found $\theta = 1/3$ which coincides with the K41 value.

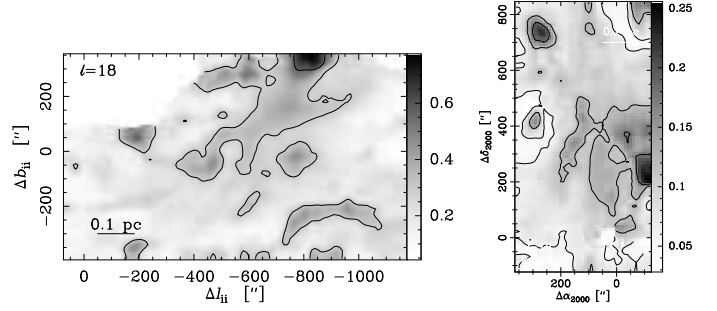


Fig. A.3. Same as Fig. 9 for a lag $l = 18$ pixels. Weak patterns are visible, reminiscent of what is seen in Fig 9. *Left panel:* contours are the 0.29 and 0.58 km s^{-1} levels. *Right panel:* contours are the 0.29 km s^{-1} with 0.29 km s^{-1} levels.

She et al. (2001) propose a method of determining the parameter β independently. It makes use of the fundamental assumption of the hierarchical SL94 model that there is a scaling law for the successive powers of the energy dissipation on scale l . Using the Kolmogorov-Oboukhov refined similarity hypothesis (RSH, see *e.g.* Lesieur 1997) $S_p \sim \langle \epsilon_l^{p/3} \rangle^{l^{1/3}}$, a recursive relation similar to Eq. A.1 can be written that involves functions of the ratio of successive orders of the S_p :

$$\mathcal{F}_l^{(p+1)} = A_p \mathcal{F}_l^{(p)\alpha} \mathcal{F}_l^{(\infty)1-\alpha} \quad (\text{A.2})$$

with $\mathcal{F}_l^{(p)} = S_{p+1}(l)/S_p(l)$. This recursive relation, together with the RSH and the second assumption that $\mathcal{F}_l^{(\infty)} \sim S_3^\gamma$, leads to the expression of the relative scaling exponents:

$$\tilde{\zeta}_p = p\gamma + (1 - 3\gamma) \frac{1 - \alpha^p}{1 - \alpha^3} \quad (\text{A.3})$$

with $\alpha = \beta^\theta$ and $\theta = 1/3$. The α -test proposed by She et al. (2001) is to plot $\mathcal{F}_l^{(p+1)}/\mathcal{F}_l^{(2)}$ against $\mathcal{F}_l^{(p)}/\mathcal{F}_l^{(1)}$ since $\mathcal{F}_l^{(p+1)}/\mathcal{F}_l^{(2)} = (A_p/A_1) (\mathcal{F}_l^{(p)}/\mathcal{F}_l^{(1)})^\alpha$. If the log-log plot is a line of slope α , the data are said to pass the α -test. In Figs. A.4-A.5, we show the result of the α -tests applied to the Polaris and Taurus data sets. Both pass the α -test with values of $\alpha = 0.89 \pm 0.01$ and 0.950 ± 0.005 for the Polaris and Taurus fields, respectively. The corresponding values of β are 0.70 ± 0.04 and 0.86 ± 0.02 in the Polaris and Taurus fields, respectively (see Figs. A.4-A.5). The intermittency level in the Polaris field is very close to the SL94 value, $\beta = 2/3$, but our data sets are too small to allow a determination of D .

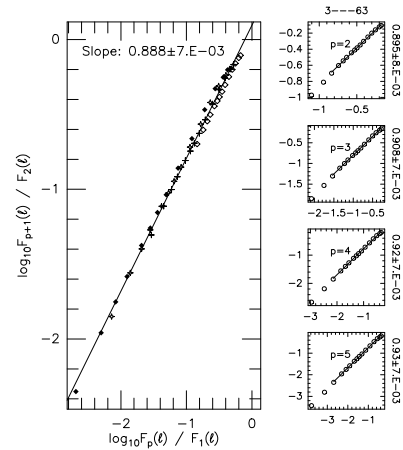


Fig. A.4. The α -test to both the Polaris field (see Appendix A.3) where $\alpha = \beta^\theta$ with $\theta = 1/3$. All orders are plotted on the left panel and fitted with a single power law, while the right panels detail the fits to individual orders $p = 2, 3, 4, 5$. Fits are done over the range indicated by the line. The individual slopes are 0.90, 0.91, 0.92 and 0.93.

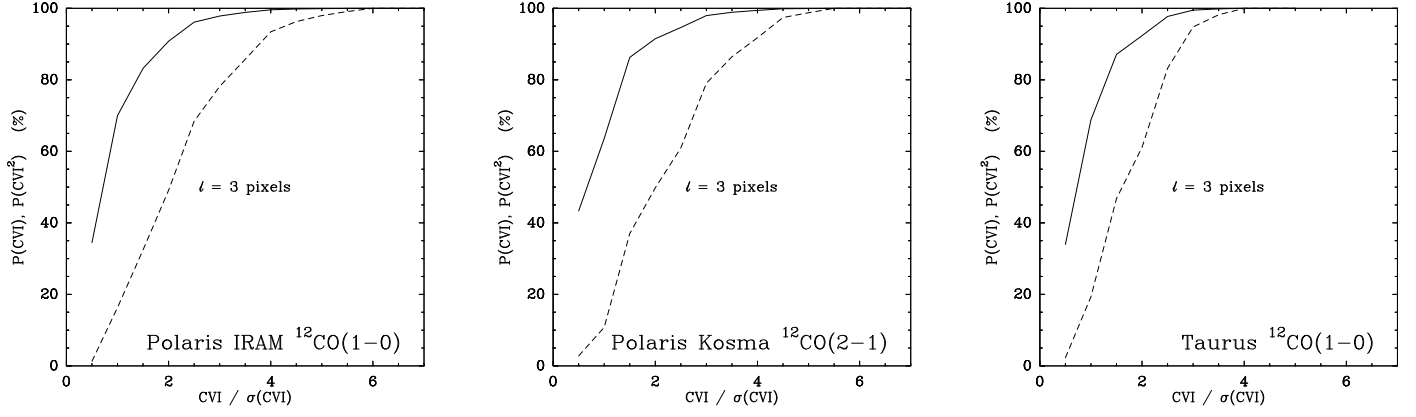


Fig. B.1. Cumulative distributions of the CVI (δC_l , full line) and the associated cumulative distributions of δC_l^2 (dashed line), shown as functions of the normalized δC_l (computed for a lag $l = 3$).

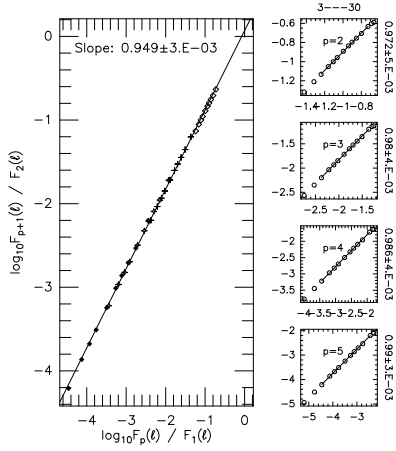


Fig. A.5. As Fig. A.4 for the Taurus field, where the slopes for each order ($p = 2, 3, 4, 5$) are 0.94, 0.95, 0.96 and 0.97.

Appendix B: Filling factor of the CVI and dissipation

Based on the PDF of CVI of Figs. 4 and 5, we computed the cumulative fraction of the CVI δC_l and the associated cumulative fraction of δC_l^2 . The non-averaged CVI δC_l are more closely related to the energy dissipation than the azimuthally averaged ones ($\langle |\delta C_l| \rangle$) because they preserve the two derivatives of the *los* velocity. The results are shown in Fig. B.1, for a lag $l = 3$. Assuming that the dissipated energy scales as δC_l^2 , we see that in the Polaris field, the regions with CVI larger than $3\sigma_{\delta C}$ represent only 2.5% of the surface and they contribute to $\approx 25\%$ of the energy dissipation. In the Taurus field, 5% of the energy dissipation is concentrated into less than 1% of the surface.